

A&A manuscript no.

(will be inserted by hand later)

Your thesaurus codes are:

03 (11.01.2; 11.09.1: Mrk 279; 11.14.1; 11.19.1; 11.06.2: molecular torus; 13.09.1)

ASTRONOMY  
AND  
ASTROPHYSICS

March 19, 2022

# Monitoring of the optical and 2.5 – 11.7 $\mu\text{m}$ spectrum and mid-IR imaging of the Seyfert 1 galaxy Mrk 279 with ISO <sup>\*</sup>

M. Santos-Lleó<sup>1</sup>, J. Clavel<sup>1</sup>, B. Schulz,<sup>2</sup> B. Altieri,<sup>1</sup> P. Barr<sup>3</sup>, D. Alloin<sup>4</sup>, P. Berlind<sup>5</sup>, R. Bertram<sup>6,7</sup>, D.M. Crenshaw<sup>8</sup>, R.A. Edelson<sup>9</sup>, U. Givon<sup>10</sup>, K. Horne<sup>11</sup>, J.P. Huchra<sup>5</sup>, S. Kaspi<sup>10</sup>, G.A. Kriss<sup>12</sup>, J.H. Krolik<sup>13</sup>, M.A. Malkan<sup>14</sup>, Yu.F. Malkov<sup>15</sup>, H. Netzer<sup>10</sup>, P.T. O'Brien<sup>9</sup>, B.M. Peterson<sup>6</sup>, R.W. Pogge<sup>6</sup>, V.I. Pronik<sup>15,16</sup>, B.-C. Qian<sup>17</sup>, G.A. Reichert<sup>18</sup>, P.M. Rodríguez-Pascual<sup>19</sup>, S.G. Sergeev<sup>15,16</sup>, J. Tao<sup>17</sup>, S. Tokarz<sup>5</sup>, R.M. Wagner<sup>6,7</sup>, W. Wamsteker<sup>20</sup>, and B.J. Wilkes<sup>5</sup>

<sup>1</sup> XMM Science Operations Center, Astrophysics Division, ESA Space Science Department, P.O. Box 50727, E-28080 Madrid, Spain

<sup>2</sup> ISO Science Operations Center, Astrophysics Division, ESA Space Science Department, P.O. Box 50727, E-28080 Madrid, Spain

<sup>3</sup> Integral Science Operations Center, Astrophysics Division, ESA Space Science Department, ESTEC, Postbus 299, 2200 AG Noordwijk, The Netherlands

<sup>4</sup> European Southern Observatory, Alonso de Cordova 3107, Vitacura Casilla 19001, Santiago 19, Chile

<sup>5</sup> Harvard-Smithsonian Center for Astrophysics, 60 Garden Street, Cambridge, MA 02138, USA

<sup>6</sup> Department of Astronomy, Ohio State University, 140 West 18th Avenue, Columbus, OH 43210, USA

<sup>7</sup> Mailing address: Steward Observatory, University of Arizona, Tucson, AZ 85721, USA

<sup>8</sup> Computer Sciences Corporation, Laboratory for Astronomy and Solar Physics, NASA Goddard Space Flight Center, Code 681, Greenbelt, MD 20771, USA

<sup>9</sup> Department of Physics and Astronomy, University of Leicester, University Road, Leicester LE1 7RH, UK

<sup>10</sup> School of Physics and Astronomy and the Wise Observatory, The Raymond and Beverly Sackler Faculty of Exact Sciences, Tel-Aviv University, Tel-Aviv 69978, Israel

<sup>11</sup> School of Physics and Astronomy, University of St. Andrews, North Haugh, St. Andrews KY16 9SS, Scotland, UK

<sup>12</sup> Space Telescope Science Institute, 3700 San Martin Drive, Baltimore, MD 21218, USA

<sup>13</sup> Department of Physics and Astronomy, The John Hopkins University, Baltimore, MD 21218, USA

<sup>14</sup> Department of Astronomy, University of California, Math-Science Building, Los Angeles, CA 90024, USA

<sup>15</sup> Crimean Astrophysical Observatory, P/O Nauchny, 334413 Crimea, Ukraine

<sup>16</sup> Isaac Newton institute of Chile, Crimean Branch

<sup>17</sup> Shanghai Astronomical Observatory, 80 Nandan Road, 200030 Shanghai, People's Republic of China

<sup>18</sup> Raytheon ITSS, Space Science Data Operations Office, NASA Goddard Space Flight Center, Code 631, Greenbelt MD 20771, USA

<sup>19</sup> Universidad Europea de Madrid, Departamento de Física, C/ Tajo sn, Urb. El Bosque, Villaviciosa de Odón, 28670 Madrid, Spain

<sup>20</sup> ESA IUE Observatory, P.O. Box 50727, 28080 Madrid, Spain

Received dd mmm yyyy / Accepted dd mmm yyyy

**Abstract.** Mid-infrared images of the Seyfert 1 galaxy Mrk 279 obtained with the ISO satellite are presented together with the results of a one-year monitoring campaign of the 2.5–11.7  $\mu\text{m}$  spectrum. Contemporaneous optical photometric and spectrophotometric observations are also presented. The galaxy appears as a point-like source at the resolution of the ISOCAM instrument (4–5"). The 2.5–11.7  $\mu\text{m}$  average spectrum of the nucleus in Mrk 279 shows

a strong power law continuum with  $\alpha = -0.80 \pm 0.05$  ( $F_\nu \propto \nu^\alpha$ ) and weak emission PAH features. The Mrk 279 spectral energy distribution shows a mid-IR bump, which extends from 2 to 15–20  $\mu\text{m}$ . The mid-IR bump is consistent with thermal emission from dust grains at a distance of  $\gtrsim 100 \text{ lt-d}$ . No significant variations of the mid-IR flux have been detected during our observing campaign, consistent with the relatively low amplitude ( $\sim 10\%$  rms) of the optical variability during the campaign. The time delay for H $\beta$  line emission in response to the optical continuum variations is  $\tau = 16.7^{+5.3}_{-5.6}$  days, consistent with previous measurements.

*Send offprint requests to:* M. Santos-Lleó

<sup>\*</sup> Based on observations collected with the Infrared Space Observatory, ISO, an ESA project with instruments funded by ESA member states (especially the PI countries: France, Germany, The Netherlands, and the United Kingdom) with the participation of ISAS and NASA.

*Correspondence to:* msantos@xmm.vilspa.esa.es

**Key words:** galaxies: active – galaxies: individual: Mrk 279 – galaxies: nuclei – galaxies: Seyfert – galaxies: molecular torus – Infrared: galaxies

## 1. Introduction

According to the unified model of active galactic nuclei (AGN), the central massive black hole, its surrounding accreting material and the broad-line region (BLR) are all embedded within a dusty region, probably a thick molecular torus. Along some directions, the dust extinction is sufficient to block all UV, optical, and near-IR radiation originating in the inner components. A review of the arguments which led to this picture is presented in Wills (1999). The presence of a universal inflection point near  $1.2\,\mu\text{m}$  in the spectral energy distribution of radio-quiet AGN's strongly suggests that the bulk of the near IR flux arises from dust thermal emission (e.g., Barvainis 1987; Sanders et al. 1989). The corresponding color temperature,  $\simeq 1,500\,\text{K}$ , matches closely the sublimation temperature of graphite, the most resilient of the grain constituents. The near IR emission can be variable, and therefore originates, at least in part, in a compact region. Furthermore, in three AGN, the near IR variations have been shown to be delayed with respect to the UV-optical variations. The time delay corresponds closely to the light-travel time to the dust sublimation radius  $r_{\text{in}}$ ; measured values of  $r_{\text{in}}$  are 400 light days for Fairall 9 (Clavel et al. 1989), 50 light days for NGC 1566 (Baribaud et al. 1992), 80 light days for NGC 3783 (Glass 1992) and 32 light days for Mrk 744 (Nelson, 1996).

The emerging picture is one where the near to mid-IR emission arises from thermal re-radiation of UV and optical photons absorbed by the circumnuclear dust. Various models for the geometry and location of this dust have been proposed, but the exact configuration of the models remains unconstrained due to a lack of suitable observational data.

One can use variability as a tool to probe the *inner* few light years of the dusty regions. Reverberation-mapping techniques (Blandford & McKee 1982) have been used extensively to map the BLR in several AGN, on scales of light days to light months, notably by the International AGN Watch<sup>1</sup> consortium (Alloin et al. 1994). A similar approach can be used to probe the IR-emitting region, i.e. the warm dust component within the obscuring material. Given UV flux variations of sufficient amplitudes, a mid-IR monitoring campaign of sufficiently long duration and adequate sampling rate, it may in principle be possible to recover the transfer function of the dust.

The Infrared Space Observatory (ISO; Kessler et al. 1996) offered a unique opportunity to carry out such

a spectrophotometric monitoring program in the mid-IR. The Seyfert 1 galaxy Mrk 279 ( $z = 0.0294$ ) was selected because its celestial position allows an uninterrupted 12-month visibility window for ISO and it has a well-documented variability history in the optical (Osterbrock & Shuder 1982; Peterson et al. 1985; Maoz et al. 1990; Stirpe et al. 1994, the UV (Chapman et al. 1985), and X-rays (Reichert et al. 1985). Balmer-line time-delays (Maoz et al. 1990; Stirpe & de Bruyn 1991; Stirpe et al. 1994) suggest a BLR size in the range 6 to 12 light days. A search for day-to-day variability across the Balmer-line profile was unsuccessful (Eracleous & Halpern 1993). No far-IR flux variations were detected with IRAS (Edelson & Malkan 1987).

## 2. IR observations and data reduction

Mrk 279 was observed with two of the instruments on board the ISO satellite: nine narrow-band filter images were obtained with ISOCAM (Cesarsky et al. 1996), while spectra were recorded with the PHT-S spectrometer, a subsystem of the ISOPHOT instrument (Lemke et al. 1996). The PHT-S spectrometer covers the  $2.5\text{--}12\,\mu\text{m}$  spectral range at a mean resolution of  $\sim 3150\,\text{km s}^{-1}$ , with a gap between  $4.9$  and  $5.9\,\mu\text{m}$ . Its entrance aperture projects to  $24'' \times 24''$  on the sky. All PHT-S observations were carried-out in an identical fashion. The integrating amplifiers were reset every 32 s and on-source measurements were interleaved with background measurements by “chopping” on the sky at a frequency of  $1/256\,\text{Hz}$ . The chopper throw was set to  $300''$ . For each of the observations, total on-source integration time was 2048 s and total observing time (including background measurements and instrument overheads) was 4236 s.

The CAM observations were performed in staring mode at a magnification of  $3''$  per pixel and with a gain of 2. Nine different filters were used. The unit integration time was 2.1 s per readout and there were between 72 and 197 readouts per image, depending on the filter used. The particular sequence of filters was chosen to go from high to low illumination so as to minimize the detector stabilization time. Good stabilization was also guaranteed by the relatively large number of readouts per exposure.

The PHT-S observations were made at 16 different epochs, from 1996, February 5 to 1997, February 13 (Table 1). The ISOCAM observations of Mrk 279 were all carried out on 1996 February 5, contemporaneously with the first of the PHT-S spectra.

Standard procedures from the CAM Interactive Analysis (CIA) software package<sup>2</sup> were used for the reduction of the ISOCAM data (Ott et al. 1997). The full width at half maximum (FWHM) of Mrk 279 varies with the filter wavelength from  $3''.3$  to  $5''.0$ , (table 2) but is always

<sup>1</sup> For a complete panorama of the AGN Watch data sets, results, and related studies, see the AGN Watch web page at URL <http://www.astronomy.ohio-state.edu/~agnwatch/>.

<sup>2</sup> CIA is a joint development by the ESA Astrophysics Division and the CAM Consortium.

consistent with that of a point source. Monochromatic intensities were obtained by integration of the source flux within a circle of radius 6 pixels ( $18''$ ) and subtraction of a normalised background measured in a concentric circular ring. The intensity of Mrk 279 in the different filters is listed in Table 2. The accuracy of these measurements is  $\pm 10\%$ .

The ISOPHOT-S data were reduced with the PHOT Interactive Analysis (PIA; <sup>3</sup> Gabriel 1998) software package. However, because ISOPHOT-S was operating close to its sensitivity limit, special reduction and calibration procedures had to be applied. After a change of illumination, the responsivity of the Si:Ga photoconductors immediately jumps to an intermediate level. This initial jump is followed by a characteristic slow transient to the final level. At the faint flux limit, this time constant is extremely long, and in practice only the initial step is observed in chopped-mode. The spectral response function for this particular mode and flux-level was derived directly from observations of a faint standard star HD 132142 whose flux ranges from 0.15 to 2.54 Jy. The calibration star observation was performed with the same chopper frequency and readout-timing as the AGN observations. The  $S/N$  of the ISOPHOT-S spectra was considerably enhanced by two additional measures: *i*) the 32-s integration ramps were divided into sub-ramps of 2 sec and no de-glitching (removal of cosmic ray hits) was performed at ramp-level *ii*) after slope-fitting and de-glitching at slope-level, the maximum of the distribution of the slopes was determined by fitting a gaussian to the histogram. The resulting ISOPHOT-S fluxes are accurate to within  $\pm 10\%$ .

The 1996 February 5 PHT-S spectrum is shown in Fig. 1, together with the monochromatic intensities measured with ISOCAM on the same day. Each PHT-S datapoint is shown with its formal error as propagated by the PIA software. The CAM and PHT-S fluxes agree to better than  $\pm 10\%$ , providing further confidence in the reliability of the flux calibration.

### 3. MIR flux Measurements and uncertainties

#### 3.1. PHT-S flux measurements and reproducibility

For each epoch of observation the continuum flux was measured over two different intervals, at short wavelengths (SW:  $2.5\text{--}4.7\ \mu\text{m}$ ) and long wavelengths (LW:  $5.8\text{--}9.9\ \mu\text{m}$ ). Table 1 lists the mean intensities over these intervals and their uncertainties, while the light curves are shown in Fig. 2.

An accurate determination of the flux uncertainties is essential when discussing source variability. We have therefore investigated the different source of errors which could potentially affect our PHT-S measurement.

<sup>3</sup> PIA is a joint development by the ESA Astrophysics Division and the ISOPHOT Consortium led by the ISOPHOT PI, D. Lemke, MPIA, Heidelberg.

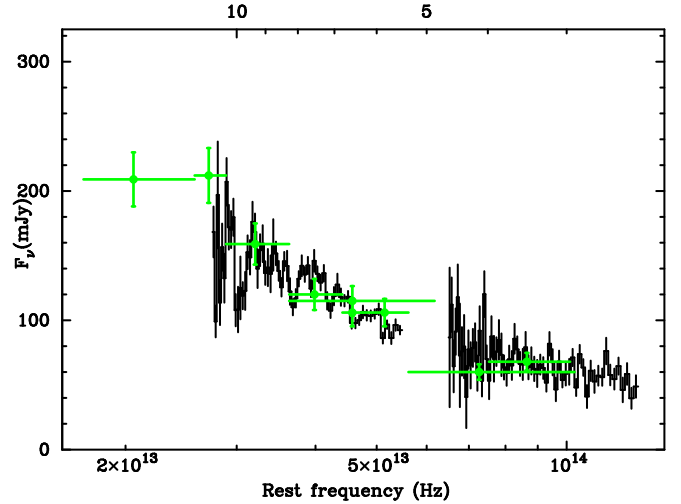


**Fig. 1.** The ISOPHOT-S spectrum from 1996 February 5 together with the ISOCAM photometric fluxes from the same date. The x-axis shows the rest frequency at the bottom and the rest wavelength in micron at the top, both on a logarithmic scale

In staring mode, the overall responsivity of PHT-S is known to remain stable within  $\pm 10\%$  (Schulz 1999). We have assessed the stability of the PHT-S responsivity more specifically at the time of each of the Mrk 279 observations and verified that no other systematic effects were present. For this purpose, two different types of calibration measurements were used as diagnostic:

1. The detector dark current measurements, which are obtained immediately prior to each PHT-S observation: throughout the campaign, the dark current signal retained its nominal value of  $\sim$  zero V/s. We can therefore be confident that none of the Mrk 279 observations suffered from detector remanence induced by a prior exposure to a bright source.
2. Measurements with an internal calibration source which are carried-out systematically at the beginning of each ISO revolution: averaged over all pixels, the variations of detector responsivity from epoch to epoch are  $\simeq \pm 2\%$ , with upper limits of 3% and 5% in the SW and LW range, respectively.

A conservative upper limit of  $\pm 10\%$  was thus adopted for the *systematic* uncertainty on the PHT-S fluxes of Mrk 279. Internal measurement errors were added in quadrature to this systematic uncertainty. The internal errors were computed as the dispersion about the mean flux in the SW and LW integration intervals, after normalization of the spectra. The purpose of the normalization is to remove the spectral curvature. Each spectrum was first divided by its best-fit power-law continuum ( $F_\nu = 8.44 \cdot 10^{-14} \nu^{-0.8} \text{ erg s}^{-1} \text{ cm}^{-2} \text{ Hz}^{-1}$ ; see §5) and the rms deviations were computed. The results show that the

internal errors associated with each flux measurement are of 2.8% and 1.7% for the 2.52–4.70  $\mu\text{m}$  and 5.76–9.89  $\mu\text{m}$  bands, respectively.

As a consistency check, errors were also computed by comparing PHT-S fluxes obtained within 30 days from each others. This gives a conservative error estimate since it assumes that there are no flux variations on time scales shorter than 30 days. Taking every pair of fluxes within 30 days and measuring the error on their means, we get mean relative errors of 3.5% and 1.6% for the SW and LW bands, respectively.

**Table 1.** PHT-S observation log and fluxes

UT	MJD	$F(2.5\text{--}4.7\ \mu)$	$F(5.8\text{--}9.9\ \mu)$
(1)	(-2,450,000)	(mJy)	(mJy)
(1)	(2)	(3)	(4)
1996 Feb 5	119	$73.5 \pm 7.6$	$132 \pm 13$
1996 Mar 3	146	$75.3 \pm 7.8$	$123 \pm 12$
1996 Mar 12	155	$65.2 \pm 6.8$	$125 \pm 13$
1996 Apr 2	176	$69.5 \pm 7.2$	$129 \pm 13$
1996 Apr 27	201	$72.7 \pm 7.6$	$127 \pm 13$
1996 May 11	215	$72.8 \pm 7.6$	$128 \pm 13$
1996 May 29	233	$73.2 \pm 7.6$	$131 \pm 13$
1996 Jul 29	294	$63.6 \pm 6.6$	$127 \pm 13$
1996 Aug 12	308	$61.8 \pm 6.4$	$122 \pm 12$
1996 Aug 27	323	$62.0 \pm 6.4$	$123 \pm 12$
1996 Sep 15	342	$60.0 \pm 6.2$	$124 \pm 13$
1996 Oct 17	374	$73.8 \pm 7.7$	$128 \pm 13$
1996 Nov 1	389	$62.6 \pm 6.5$	$120 \pm 12$
1996 Nov 18	406	$73.7 \pm 7.7$	$128 \pm 13$
1996 Dec 5	423	$70.1 \pm 7.3$	$124 \pm 13$
1997 Feb 13	493	$81.8 \pm 8.5$	$128 \pm 13$

**Table 2.** ISOCAM narrow band filter intensities

Filter	$\lambda_c$	Range	Flux	FWHM
	( $\mu\text{m}$ )	( $\mu\text{m}$ )	(mJy)	( $''$ )
(1)	(2)	(3)	(4)	(5)
SW1	3.57	3.05–4.10	68	3.9
SW5	4.25	3.00–5.5	60	3.3
LW4	6.00	5.50–6.50	106	4.1
LW2	6.75	5.00–8.50	115	4.8
LW5	6.75	6.50–7.00	106	4.2
LW6	7.75	7.00–8.50	120	5.0
LW7	9.62	8.50–10.7	159	3.8
LW8	11.4	10.7–12.0	212	4.5
LW3	15.0	12.0–18	209	5.0

### 3.2. Comparison with ground based measurements and estimation of the host galaxy contribution

Spinoglio et al. (1985) measured  $L$ -band ( $\sim 3.5\ \mu\text{m}$ ) fluxes of  $100 \pm 21\ \text{mJy}$ ,  $112 \pm 27\ \text{mJy}$ , and  $68 \pm 15\ \text{mJy}$  through apertures of  $12''$ ,  $12''$ , and  $17''$ , respectively, consistent with our results to within the measurement uncertainties.

Given the spectrograph aperture ( $24'' \times 24''$ ), the host galaxy of Mrk 279 could, in principle, contribute to the PHT-S flux. Indeed, a faint extended nebulosity is apparent in the  $K$ -band ( $\sim 2.2\ \mu\text{m}$ ) image of McLeod & Rieke (1995). This extended flux arises from the integrated emission of giants and supergiants in the galactic disk whose energy distribution is maximum at  $\sim 2\ \mu\text{m}$  and falls-off abruptly at longer wavelengths. In practice, stellar emission will therefore make a negligible contribution to the PHT-S flux. Nevertheless, this was positively verified by comparison with ground-based data as follows:

1. In the  $K$ -band, McLeod & Rieke (1995) estimated that the AGN contributes 90% of the flux within the central  $1''.5$  (FWHM) and 55% (35 mJy) of the total  $K$ -band flux (68 mJy) integrated over the whole galaxy (i.e., out to a radius of  $35''$ ). Assuming “normal” near-IR colors ( $K - L = 0.22 \pm 0.02\ \text{mag}$ ; Clavel et al. 1989) for the stellar population, we derive a total host-galaxy flux of 18 mJy at  $3.5\ \mu\text{m}$ .
2. Using the  $B$ - and  $R$ -band nucleus–galaxy decomposition of Granato et al. (1993), and assuming normal optical-to-IR ( $V - K = 3.22\ \text{mag}$ ; Clavel et al. 1989) and  $K - L$  colors, we estimate a total galaxy flux of 20 mJy and 17 mJy respectively at  $3.5\ \mu\text{m}$ .

These consistent estimates can be used to infer the amount of stellar light which enters the  $24'' \times 24''$  PHT-S aperture,  $5 \pm 2\ \text{mJy}$  at  $3.5\ \mu\text{m}$  flux. Such a small contamination is within the measurement errors and can be neglected.

The galaxy contributes  $11 \pm 4\ \text{mJy}$ ,  $14 \pm 5\ \text{mJy}$  and  $11 \pm 4\ \text{mJy}$  to the  $12''$  photometric measurements in the  $J$ ,  $H$ , and  $K$  bands respectively (Granato et al. 1993). These values are used in §6 to infer the intrinsic spectral energy distribution of the active nucleus in Mrk 279

## 4. Optical observations and data reduction

Ground-based optical observations were made in support of the ISO observations. Spectroscopic monitoring was carried out with the 1.8-m Perkins Telescope of the Ohio State and Ohio Wesleyan University at the Lowell Observatory, the 1.0-m telescope of the Wise Observatory, the 2.6-m Shajn Telescope of the Crimean Observatory, and the 1.5-m Mt. Hopkins Telescope of the Harvard-Smithsonian Center for Astrophysics (CfA). A detailed log of the spectroscopic observations can be found at the International AGN Watch website.

In addition CCD photometry was made on the 1.0-m telescope of the Wise Observatory. The flux was measured

using a fixed aperture of radius  $7''$ , under seeing conditions of  $2-3''$ . The  $B$ ,  $V$ ,  $R$ , and  $I$  instrumental magnitudes are listed in columns (3) – (6) of table 4. They have not been scaled to any standard system.

The spectroscopic data were processed by the individual observers in standard fashion for CCD frames. However, the standard astronomical flux calibration techniques based on determining the instrument response function from observations of standard stars are only accurate for AGN spectrophotometry at about the 10% level even under ideal observing conditions. We used the standard stars only for *relative* calibration, and employed different calibration techniques for absolute calibration: The data from Wise Observatory were calibrated following the method described by Maoz et al. (1994). The data from Ohio, Crimean, and CFA were calibrated through scaling through  $[\text{O III}] \lambda 5007$  flux that was measured on five photometric nights, at  $F([\text{O III}] \lambda 5007) = (1.512 \pm 0.096) \times 10^{-13} \text{ ergs s}^{-1} \text{ cm}^{-2}$ .

On these calibrated spectra we measured the continuum flux by averaging the flux in a  $10 \text{ \AA}$  wide band centered at  $5105 \text{ \AA}$  in the rest frame of Mrk 279 ( $F_\lambda(5100 \text{ \AA})$ ). The  $\text{H}\beta$  line flux has been measured by linear interpolation between rest-frame wavelengths  $\sim 4765 \text{ \AA}$  and  $\sim 5105 \text{ \AA}$ , and line integration between  $4770 \text{ \AA}$  and  $4935 \text{ \AA}$ . The long-wavelength cutoff of this integration band misses some of the  $\text{H}\beta$  flux underneath  $[\text{O III}] \lambda 4959$ , but avoids the need to estimate the  $\text{Fe II}$  contribution to this feature and still gives a good representation of the  $\text{H}\beta$  variability. We did not correct for the narrow-line, which is expected to be constant.

As the measurements made from the spectra are subject to systematic differences between the four data sets used, we applied the prescriptions of Peterson et al. (1999) to intercalibrate the data sets, and correct for aperture effects. The final continuum  $F_\lambda(5100 \text{ \AA})$  and  $\text{H}\beta$  emission-line fluxes are given in table 5. The spectrophotometric and photometric light curves are shown in Fig. 2. Using the results of Granato et al. (1993), we estimate that stars contribute for  $1.2 \pm 0.6 \text{ mJy}$  or  $20 \pm 10\%$  to the mean reddening corrected  $5100 \text{ \AA}$  flux.

## 5. The mid-IR spectrum of Mrk 279

Figure 3 shows the weighted mean  $2.5 - 11.7 \text{ \mu m}$  spectrum of Mrk 279 obtained by averaging all 16 PHT-S spectra.

The spectrum of Mrk 279 is quite similar to the mean Seyfert 1 spectrum obtained by Clavel et al. (2000) from their sample of 28 type 1 AGNs. It shows a strong continuum, with a flux density per frequency unit that drops sharply with increasing frequency and only weak broad emission features. The continuum is well approximated by a power law ( $F_\nu \propto \nu^\alpha$ ) of spectral index  $\alpha = -0.80 \pm 0.05$  (Fig. 3), close to the average Seyfert 1 mid-IR index  $\alpha = -0.84 \pm 0.24$  (Clavel et al. (2000)). Its flux at a fiducial wavelength of  $7 \text{ \mu m}$  is  $103 \text{ mJy}$ . While the broad emis-

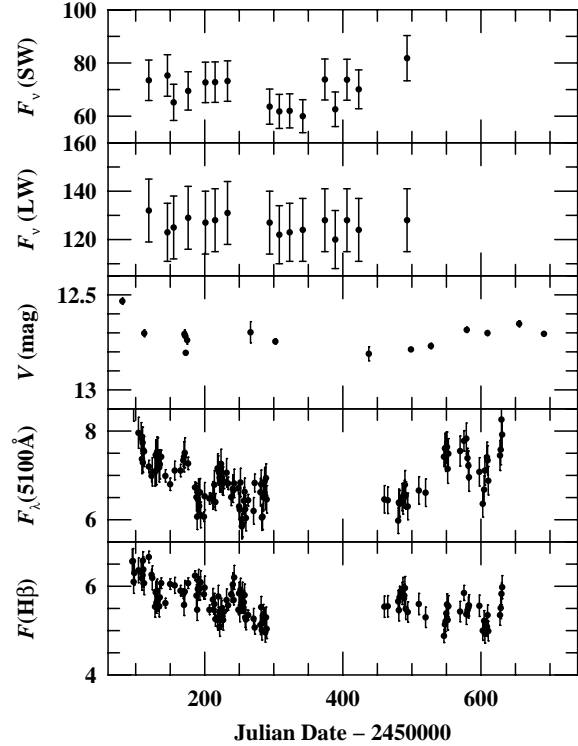


**Fig. 2.** IR and optical light curves of Mrk 279. The top two panels show the IR light curves from the SW and LW detectors ( $2.52-4.70 \text{ \mu m}$  and  $5.8-9.9 \text{ \mu m}$ , respectively). The third panel shows  $V$ -band photometric measurements from Wise Observatory. The fourth panel shows the  $5100 \text{ \AA}$  continuum flux measured from the spectra, in units of  $10^{-15} \text{ ergs s}^{-1} \text{ cm}^{-2} \text{ \AA}^{-1}$ . The  $\text{H}\beta$  flux is shown in the bottom panel, in units of  $10^{-13} \text{ ergs s}^{-1} \text{ cm}^{-2}$ . The optical photometry, optical continuum and  $\text{H}\beta$  fluxes are available in electronic form at the CDS.

sion features of Polycyclic Aromatic Hydrocarbon (PAH) bands (Puget et al. 1985) at  $3.3 \text{ \mu m}$ ,  $6.2 \text{ \mu m}$ ,  $7.7 \text{ \mu m}$ , and  $8.6 \text{ \mu m}$  are ubiquitous in many different galactic and extragalactic line of sight, only the strongest band at  $7.7 \text{ \mu m}$  is unambiguously detected in Mrk 279, with an intensity of  $0.76 \pm 0.12 \text{ mJy}$ . Clavel et al. (2000) showed that PAH emission in AGNs originates in the interstellar medium (ISM) of the galaxy, whereas the mid-IR power-law continuum arises from near nuclear dust emission in the torus. Because Mrk 279 is a luminous AGN, almost a quasar, the apparent weakness of its PAH emission can be understood as a contrast effect whereby a faint ISM is observed against a bright nucleus. The  $9.7 \text{ \mu m}$  silicate absorption feature, conspicuous in the mid-IR spectra of starburst galaxies (Moorwood et al. 1996; Rigopoulou et al. 1996; Acosta-Pulido et al. 1996), is absent from the Mrk 279 spectrum.

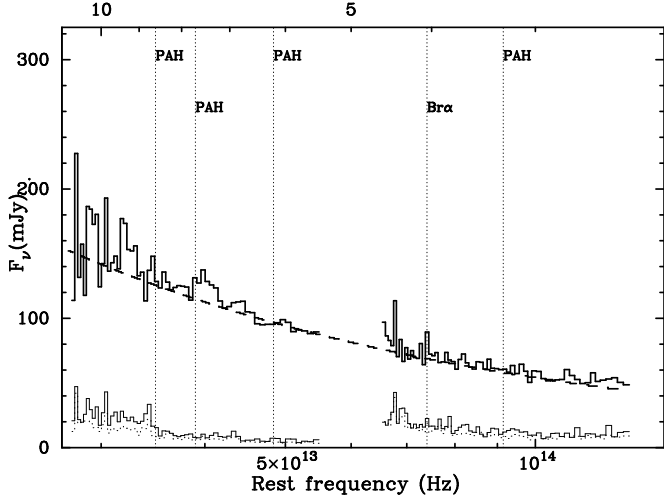


**Fig. 3.** The weighted averaged mid-IR spectrum of Mrk 279 (dark line), the rms deviations about the mean (light line) and the error (dotted line). The best-fit power law with index  $\alpha = -0.8$  is shown as a dashed line. The expected positions of PAH and Br $\alpha$  features are indicated. The x-axis shows the rest frequency at the bottom and the rest wavelength, in microns, at the top, both represented on a logarithmic scale

## 6. The spectral energy distribution

Figure 4 shows the continuum spectral energy distribution (SED) of Mrk 279 from the far-IR to the X-rays. The IRAS data points are the average of 6 pointed observations reported by Edelson & Malkan (1987). The near-IR data are from Spinoglio et al. (1985) after subtraction of the stellar light (§3.2). The *R* and *B* band fluxes (Granato et al. 1993) and the mean 5100 Å-flux (this paper) have also been corrected for the underlying galaxy contribution and de-reddened. The 1500 Å data point represents the average of 26 observations made with IUE (Rodríguez et al. 1998) between 1978 and 1991. It has been corrected for foreground reddening using  $N_H = 1.6 \times 10^{20} \text{ cm}^{-2}$  (Elvis et al. 1989). The large error bar reflects the strong variability of Mrk 279 at UV wavelengths. The EXOSAT X-ray data are from 1983 and 1984 and are best described in terms of a broken power-law (Ghosh & Soundararajaperumal 1992), while the 1994 data from ASCA are modeled with a unique power law in the Tartarus Database (<http://tartarus.gsfc.nasa.gov/>).

Since this SED is constructed from data collected over  $\sim 19$  years, we caution that it may be distorted by variability. Variability is important in shaping the X-ray, ultraviolet, and optical spectrum, but is much less significant at longer wavelengths (see §7). Bearing these limitations in mind, it is still possible to draw some general conclusions which are not affected by flux variations at short wavelengths.

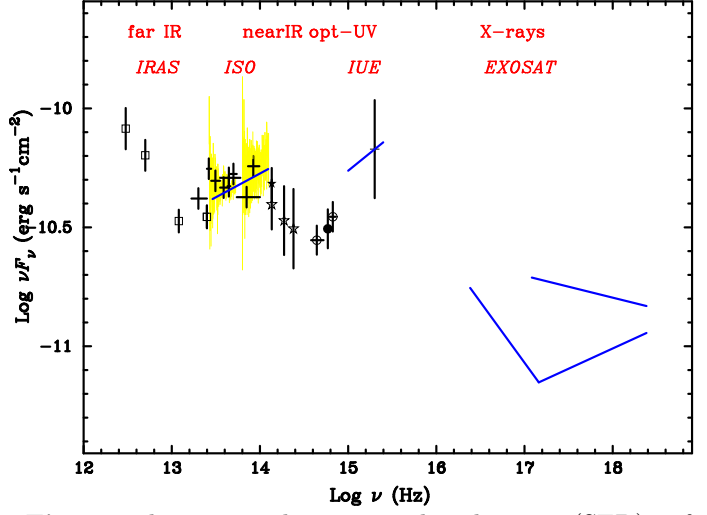


**Fig. 4.** The spectral energy distribution (SED) of Mrk 279, from the far-IR to the X-rays. The IRAS data are represented as open squares whereas near-IR ground-based data are shown as stars. The PHT-S spectrum is shown as a dotted line, while ISOCAM fluxes are plotted as crosses where the horizontal bars indicate the filter range. The two open circles in the optical are the *nuclear R*- and *B*-band fluxes. The filled circle is the mean 5100 Å flux. Optical and near IR data have been corrected for stellar light while UV and optical data have been corrected for galactic reddening. The best fit power laws mid-IR and UV ( $\alpha = -0.7$ ) continua are also displayed. The error bar on the UV flux represents the rms fluctuation about the mean 1500 Å due to variability. This SED was assembled from data gathered over a time span of  $\sim 19$  years.

The Mrk 279 SED displays three broad maxima or “bumps”. The first maximum occurs in the far-IR at wavelengths  $\geq 25 \mu\text{m}$ . Given the large IRAS ( $\sim 1'$ ) apertures and the cold color temperature of the far-IR bump, the 100  $\mu\text{m}$  and 60  $\mu\text{m}$  fluxes are probably dominated by cold dust from the host galaxy’s ISM. Hence, the far-IR “bump” is most likely not related to the AGN itself. The second maximum is the usual “big blue bump” which dominates the SED of type 1 AGNs from the optical to the soft X-rays. It is usually identified as thermal emission from an accretion disk. In between these two maxima lies a third and smaller bump which extends from  $\sim 1 \mu\text{m}$  to  $\sim 15\text{--}20 \mu\text{m}$ . We tentatively identify this mid-IR bump as thermal emission from dust in the putative molecular torus and/or from dust in the NLR, as discussed below.

## 7. The IR variability

The total duration of our ISO campaign was 374 days, with a mean sampling interval of 24.9 days. In addition to the weighted-mean spectrum,  $\langle F_\nu \rangle$ , Fig. 3 displays the

rms spectrum  $\langle \text{rms}_\nu \rangle$ , and the mean error spectrum  $\epsilon_\nu$ . The latter was evaluated as

$$\epsilon_\nu^2 = \frac{1}{N \sum_{i=1}^N 1/\Delta_{\nu,i}^2} \quad (1)$$

where  $\Delta_{\nu,i}$  is the uncertainty associated with the flux  $F_i$  at epoch  $i$  and  $N = 16$  is the number of epochs. We can exclude significant (i.e.  $3\sigma$ ) flux variability since the largest value of  $\langle \text{rms}_\nu \rangle / \epsilon_\nu$  is only  $\approx 1.4$ . A chi-square test was also applied to the average PHT-S fluxes of Table 1. The reduced chi-squares are  $< 1$  which confirms that no significant variations of the mid-IR flux took place during our  $\sim 1$ -year observing campaign.

## 8. Optical variability and the H $\beta$ emission-line lag

The relatively dense sampling of the optical light curves between January and July 1996 allows us to measure the time-delayed response, or “lag”, of the H $\beta$  emission line to continuum variations by cross-correlation of the light curves shown in Fig. 2. We used both the interpolation method of Gaskell & Sparke (1986) and the discrete-correlation function (DCF) method of Edelson & Krolik (1988), in both cases employing the specific implementation described by White & Peterson (1994). The centroid of the cross-correlation is at  $16.7_{-5.6}^{+5.3}$  days. Uncertainties were estimated using the model-independent FR/RSS Monte-Carlo method described by Peterson et al. (1998). The cross-correlation results are shown in Table 3 and Fig. 5. For comparison, Table 3 also lists the results of previous Mrk 279 monitoring campaigns by Maoz et al. (1990) and Stirpe et al. (1994).

## 9. Discussion and concluding remarks

The mid-IR spectrum of Mrk 279 shows a strong power-law continuum of spectral index  $-0.80 \pm 0.05$ , with weak PAH emission bands and no detectable silicate  $\sim 9.7 \mu\text{m}$  feature. The mid-IR bump of Mrk 279 extends<sup>4</sup> from roughly  $1.25 \mu\text{m}$  to  $15\text{--}20 \mu\text{m}$  and is wider than a single blackbody. It peaks near  $\approx 3 \mu\text{m}$ . In Fairall 9, the mid-IR bump most likely originates from the re-processing of UV and optical photons by nuclear dust (§1). We can estimate the distance to the central source of the innermost and hottest dust grains in Mrk 279,  $r_{\text{in}}$ , by scaling directly from Fairall 9 (Clavel et al. 1989). Mrk 279 is approximately eight times less luminous than Fairall 9. Since the inner radius of the dust distribution is presumably controlled by sublimation,  $r_{\text{in}}$  should scale approximately as  $L^{1/2}$ , so  $r_{\text{in}}$  should be a factor of  $\simeq 2.8$  smaller in Mrk 279 than in Fairall 9, i.e.  $r_{\text{in}} \approx 140 \pm 36$  light-days.

<sup>4</sup> for the extension of the bump we consider the wavelength range  $\Delta\lambda$  over which  $\nu F_\nu$  exceeds one third of its peak value.

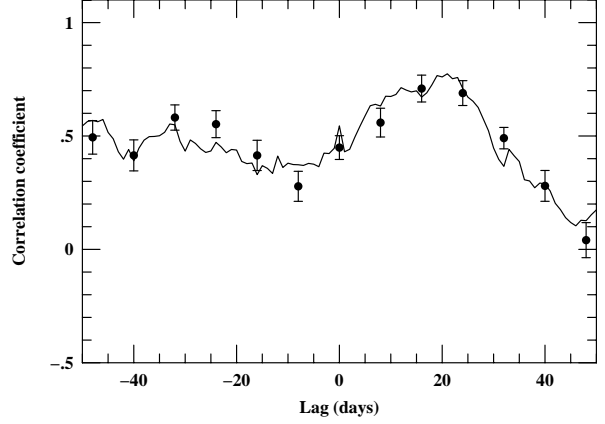


**Fig. 5.** Cross-correlation function of the H $\beta$  line intensity versus the 5100 Å optical continuum flux between JD 2,450,095.1 and JD 2,450,289.7 (Fig. 2). The interpolation CCF is shown as a solid line and the points with error bars are computed using the DCF method (with a bin size of 8 days). The H $\beta$  line lags behind the continuum by about 16 days.

During the ISO campaign, the mid-IR flux did not experience variations of amplitude larger than 10 %, the detection limit of the PHT-S instrument. Optical data contemporaneous to the IR observations revealed significant fluctuations of the 5100 Å flux with a relative rms amplitude of 9% and a ratio of the maximum to the minimum fluxes,  $R_{\text{max}} \sim 1.64 \pm 0.11$ . Any upper limit to the mid-IR variability in Mrk 279 has to be examined in the light of the UV and optical continuum variations over the same period of time. As noted earlier, in the dust reprocessing scenario the amplitude of the MIR flux variations will be reduced compared to that of the primary UV-optical source because of the finite propagation time of the photons. Imagine a short (duration  $\leq 1$  day) pulse of the UV-optical source illuminating a thin dust annulus, inclined by  $i = 10^\circ$  with respect to the line of sight. The annulus IR response will be delayed by  $\delta t = (1 - \sin i)r_{\text{in}}/c$  and will last for  $2(\sin i)r_{\text{in}}/c$ . For numerical values appropriate to Mrk 279, the duration of the IR reverberated pulse will be 38 days and its peak amplitude thereby reduced by a factor of order 38. Given the relatively low amplitude of the optical flux variations (Fig. 2), the absence of measurable variations of the MIR flux is consistent with the above scenario.

Though a detailed quantitative fit with a particular model is beyond the scope of this paper, it is nevertheless illustrative to perform a qualitative comparison of our data with the theoretical predictions from the torus model by Pier & Krolik (1992). This model predicts a mid-IR “bump” that is approximately 0.7 to 1 decade wide in



**Table 3.** Cross-Correlation Results

Parameter (1)	This Work (H $\beta$ ) (1996) (2)	Wise Obs.(H $\beta$ ) (1988) (3)	Wise Obs.(H $\alpha$ ) (1988) (4)	LAG (H $\alpha$ ) (1990) (5)
Cross-correlation centroid $\tau_{\text{cent}}$ (days)	$16.7^{+5.3}_{-5.6}$	$2.5^{+25.5}_{-5.4}$	$11.6^{+8.5}_{-11.7}$	$6.8^{+19.8}_{-6.9}$
Cross-correlation peak $\tau_{\text{peak}}$ (days)	$21^{+2}_{-9}$	$3^{+28}_{-5}$	$11^{+11}_{-11}$	$2^{+29}_{-3}$
Peak correlation coefficient $r_{\text{max}}$	0.769	0.799	0.793	0.795
Continuum rms fractional variability $F_{\text{var}}$	0.093	0.071	0.071	0.126
Mean time between observations (days)	2.3	4.1	4.1	6.0
Duration of campaign (days)	195	156	156	152

wavelengths, in agreement with the Mrk 279 observations. In the Pier & Krolik (1992) model, the torus emission is expected to peak at a wavelength  $\lambda_{\text{peak}}$  that depends primarily on the flux illuminating the torus inner surface and its inclination angle  $i$  with respect to the line of sight. The relatively high color temperature implied by  $\lambda_{\text{peak}} \approx 3 \mu\text{m}$  constrains the inclination to be small ( $\cos i \geq 0.75$ ). The absence of silicate absorption also rules-out very optically thick models and constrains the vertical column density at the torus inner edge,  $N_{\text{H}} \leq 10^{24} \text{ cm}^{-2}$ . Comparison of Fig. 4 with Fig. 5 of Pier & Krolik (1992) also suggests a moderately thick torus, with  $r_{\text{in}}/h = 0.3$ .

The delay  $\Delta T$  of H $\beta$  w.r.t. the optical continuum was  $16.7^{+5.3}_{-5.6}$  days during this campaign. Comparison with the results from previous monitoring campaigns (see Table 3) does not reveal any significant change of  $\Delta T$  over a time span of  $\sim 8$  years. In other words, we find no evidence for a secular change in the structure of the BLR in Mrk 279. Equating  $c \times \Delta T$  with the emissivity weighted radius  $R_{\text{BLR}}$  of the H $\beta$  emitting region, one sees that  $r_{\text{in}}$  is about 8 times larger than  $R_{\text{BLR}}$ . In other words, the BLR lies well within the dust evaporation radius.

**Acknowledgements.** The authors are grateful to all the observatories involved for the generous allocation of observing time and José Acosta-Pulido for helpful discussions on the PHT-S instrument calibration. MS acknowledges partial support by Spanish CICYT grant PB-ESP95-0389-C02-02 and all the staff at the *Laboratorio de Astrofísica Espacial y Física Fundamental*, Spain where most of this work was done. Support for the ground-based observations was provided by the National Science Foundation through grant AST-9420080 to Ohio State University. Observations at the Wise Observatory are supported by grants from the Israel Science Foundation. This research has made use of the TARTARUS database, which is supported by Jane Turner and Kirpal Nandra under NASA grants NAG5-7385 and NAG5-7067.

## References

Acosta-Pulido J.A., Klaas U., Laureijs R.J., et al. 1996, A&A 315, L125  
 Alloin D., Clavel J., Peterson B.M., Reichert G.A., Stirpe G.M., 1994, in *Frontiers of Space and Ground-Based Astronomy*, ed. W. Wamsteker, M.S. Longair, Y. Kondo (Dordrecht:Kluwer) p. 423  
 Baribaud T., Alloin D., Glass I., Pelat D., 1992, A&A 256, 375

Barvainis R., 1987, ApJ 320, 537  
 Blandford R.D., McKee C.F., 1982, ApJ 255, 419  
 Chapman G.N., Geller M.J., Huchra J.P., 1985, ApJ 297, 151  
 Cesarsky C.J., Abergel A., Agnese P., et al. 1996, A&A 315, L32  
 Claussen M.J., Lo K.Y., 1986, ApJ 308, 592  
 Clavel J., Wamsteker W., Glass I., 1989, ApJ 337, 236  
 Clavel J., et al., 2000, A&A 357, 839.  
 Edelson R.A., Krolik J.H. 1988, 333, 646  
 Edelson R.A., Malkan M., 1987, ApJ 323, 516  
 Elvis M., Lockman F.J., Wilkes B.J., 1989, AJ 97, 777  
 Eracleous M., Halpern J., 1993, ApJ 409, 584  
 Gabriel, C. 1998, PHOT Interactive Analysis Users Manual, 3rd ed., <http://www.iso.vilspa.esa.es/manuals>  
 Gaskell C.M., Sparke L.S. 1986, ApJ 305, 175  
 Ghosh K.K., Soundararajaperumal S., 1992, MNRAS 259, 175  
 Glass I., 1992, MNRAS 256, 23P  
 Granato G.L., Zitelli V., Bonoli F., Danese L., Bonoli C., Delpino F., 1993, ApJS 89, 35  
 Kessler M.F., Steinz J.A., Anderegg M.E., et al., 1996, A&A 315, L27  
 Lacy J.H., Soifer B.T., Neugebauer C., et al., 1982, ApJ 256, 75  
 Lemke D., Klaas U., Abolins J., et al. 1996, A&A 315, L61  
 Maoz D., Netzer H., Leibowitz E., et al. 1990, ApJ 351, 75  
 Maoz D., Smith P.S., Jannuzi B., Kaspi S., Netzer H. 1994, ApJ 421, 34  
 Marco O., Alloin D., Beuzit J.L., 1997, A&A 320, 399  
 Marco O., Alloin D., 2000, A&A 353, 465.  
 McLeod K.K., Rieke G.H., 1995, ApJ 441, 96  
 Moorwood A.F.M., Lutz D., Oliva E., Marconi A., Netzer H., Genzel R., Sturm E., de Graauw T., 1996, A&A 315, L109  
 Osterbrock D.E., Shuder J.M., 1982, ApJS 49, 149  
 Ott S., Abergel A., Altieri B., et al. 1997, Design and Implementation of CIA, the ISOCAM Interactive Analysis System, I: Hunt G., Payne H.E. (eds) ASP Conf. Series Vol. 125, p. 34  
 Peterson B.M., Crenshaw D.M., Meyers K.A., 1985, ApJ 298, 283  
 Peterson B.M., Wanders I., Horne K., Collier S., Alexander T., Kaspi S., Maoz D. 1998, PASP 110, 660  
 Peterson B.M., Barth A.J., Berlind P., et al. 1999, ApJ 510, 659  
 Pier E.A., Krolik J.H., 1992, ApJ 401, 99  
 Puget J.L., Leger A., Boulanger F., 1985, A&A 142, L19  
 Reichert G.A., Mushotzky R.F., Petre R., Holt S.S., 1985, ApJ 296, 69  
 Rigopoulou D., Lutz D., Genzel R., et al. 1996, A&A 315, L121



- Rodríguez-Pascual P.M., González-Riestra R., Schartel N., Wamsteker W., 1999, A&AS 139, 183
- Rouan D., Rigaut F., Alloin D., et al. 1998, A&A 339, 687
- Sanders B., Phinney E. S., Neugebauer G., Soifer B. T., Matthews K., 1989, Apj 347, 29
- Schulz B., 1999, “The long term responsivity stability of ISOPHOT-S”, ISO internal report, 28 May 1999, [http://www.iso.vilspa.esa.es/users/expl\\_lib/PHT\\_list.html](http://www.iso.vilspa.esa.es/users/expl_lib/PHT_list.html)
- Spinoglio L., Persi P., Ferrari-Yoniolo M., et al., 1985, A&A 153, 55
- Stirpe G.M., de Bruyn A.G., 1991, A&A 245, 355
- Stirpe G.M., Alloin D., Axon D.J., et al. 1994, A&A 285, 857
- van Groningen E., Wanders I. 1992, PASP 104, 700
- Veilleux S., Goodrich R.W., Hill G.J., 1997, ApJ 477, 631
- White R.J., Peterson B.M. 1994, PASP 106, 879
- Wills, B., 1999, in Quasars and Cosmology, ed. G. Ferland and J. Baldwin, Astronomical Society of the Pacific Conference Series, vol 162, p. 101.

## Electronic tables

**Table 4.** Optical Photometry from Wise Observatory

UT Date (1)	Julian Date (−2, 450, 000) (2)	$B^*$ (mag) (3)	$V^*$ (mag) (4)	$R^*$ (mag) (5)	$I^*$ (mag) (6)
1995 Dec 28	80.6	$13.838 \pm 0.020$	$12.533 \pm 0.016$	$12.461 \pm 0.012$	
1996 Jan 29	112.4	$14.111 \pm 0.040$	$12.702 \pm 0.018$	$12.578 \pm 0.010$	$12.771 \pm 0.022$
1996 Mar 27	170.6	$14.097 \pm 0.015$	$12.706 \pm 0.022$	$12.588 \pm 0.016$	
1996 Mar 28	171.5	$14.070 \pm 0.021$	$12.715 \pm 0.022$	$12.605 \pm 0.012$	
1996 Mar 29	172.5	$14.151 \pm 0.013$	$12.805 \pm 0.005$	$12.699 \pm 0.006$	
1996 Mar 31	174.5	$14.110 \pm 0.024$	$12.738 \pm 0.021$	$12.631 \pm 0.023$	$12.829 \pm 0.023$
1996 May 2	206.5	$14.517 \pm 0.015$	$13.243 \pm 0.014$	$13.130 \pm 0.012$	$13.426 \pm 0.026$
1996 Jul 1	266.3	$14.377 \pm 0.042$	$12.697 \pm 0.056$	$12.733 \pm 0.098$	
1996 Jul 2	267.3	$14.417 \pm 0.030$		$12.762 \pm 0.051$	$12.964 \pm 0.080$
1996 Aug 6	302.2	$14.111 \pm 0.017$	$12.745 \pm 0.014$	$12.626 \pm 0.017$	$12.831 \pm 0.018$
1996 Dec 19	437.6	$14.245 \pm 0.045$	$12.810 \pm 0.037$	$12.659 \pm 0.022$	$12.837 \pm 0.012$
1997 Feb 18	498.6	$14.192 \pm 0.013$	$12.787 \pm 0.008$	$12.673 \pm 0.019$	$12.856 \pm 0.024$
1997 Mar 19	527.5	$14.179 \pm 0.019$	$12.769 \pm 0.014$	$12.661 \pm 0.009$	$12.842 \pm 0.021$
1997 May 10	579.4	$14.090 \pm 0.027$	$12.684 \pm 0.014$	$12.576 \pm 0.009$	$12.776 \pm 0.013$
1997 Jun 9	609.4	$14.088 \pm 0.021$	$12.701 \pm 0.013$	$12.604 \pm 0.012$	
1997 Jul 25	655.3	$14.005 \pm 0.028$	$12.652 \pm 0.016$	$12.550 \pm 0.021$	$12.770 \pm 0.013$
1997 Aug 30	691.3	$14.118 \pm 0.030$	$12.705 \pm 0.010$	$12.578 \pm 0.020$	

★ Instrumental magnitudes, not scaled to any standard system

**Table 5.** Optical Continuum and H $\beta$  fluxes

Julian Date (−2, 450, 000)	$F_{\lambda}$ (5100 Å)	$F(\text{H}\beta)$
(1)	(a) (2)	(b) (3)
95.1	$9.39 \pm 0.40$	$6.56 \pm 0.28$
96.0	$9.67 \pm 0.41$	$6.57 \pm 0.28$
97.0	$8.59 \pm 0.37$	$6.10 \pm 0.26$
98.1	$9.09 \pm 0.39$	$6.30 \pm 0.27$
104.0	$7.96 \pm 0.35$	$6.36 \pm 0.28$
108.0	$7.84 \pm 0.35$	$6.32 \pm 0.27$
109.0	$7.37 \pm 0.33$	$6.18 \pm 0.27$
110.0	$7.74 \pm 0.35$	$6.25 \pm 0.27$
110.4	$7.29 \pm 0.22$	$6.58 \pm 0.20$
111.0	$7.57 \pm 0.34$	$6.38 \pm 0.28$
112.1	$7.54 \pm 0.34$	$6.07 \pm 0.26$
119.0	$7.20 \pm 0.14$	$6.66 \pm 0.13$
123.0	$6.99 \pm 0.14$	$6.26 \pm 0.12$
124.0	$7.08 \pm 0.32$	$6.19 \pm 0.27$
128.0	$7.08 \pm 0.32$	$5.54 \pm 0.24$
129.0	$7.46 \pm 0.34$	$5.86 \pm 0.25$
130.0	$7.12 \pm 0.33$	$5.63 \pm 0.24$
131.0	$7.53 \pm 0.34$	$5.90 \pm 0.26$
132.0	$7.51 \pm 0.34$	$5.69 \pm 0.25$
134.0	$7.18 \pm 0.33$	$5.55 \pm 0.24$
134.9	$7.25 \pm 0.33$	$5.75 \pm 0.25$
136.9	$7.42 \pm 0.15$	$6.07 \pm 0.12$
143.0	$6.99 \pm 0.14$	$5.62 \pm 0.11$
149.9	$6.80 \pm 0.14$	$6.05 \pm 0.12$
156.5	$7.11 \pm 0.21$	$6.02 \pm 0.18$
164.9	$7.11 \pm 0.14$	$5.90 \pm 0.12$
168.9	$7.34 \pm 0.14$	$5.83 \pm 0.11$
170.0	$7.42 \pm 0.34$	$5.58 \pm 0.24$
171.0	$7.51 \pm 0.34$	$5.88 \pm 0.25$
175.9	$7.27 \pm 0.14$	$6.07 \pm 0.12$
185.9	$6.73 \pm 0.12$	$6.24 \pm 0.11$
188.0	$6.51 \pm 0.31$	$5.79 \pm 0.25$
189.0	$6.07 \pm 0.29$	$5.47 \pm 0.24$
190.0	$6.46 \pm 0.31$	$5.94 \pm 0.26$
191.0	$6.61 \pm 0.31$	$6.12 \pm 0.26$
191.9	$6.31 \pm 0.12$	$5.96 \pm 0.11$
193.0	$6.62 \pm 0.31$	$5.95 \pm 0.26$
194.0	$6.11 \pm 0.29$	$6.09 \pm 0.26$
198.8	$6.07 \pm 0.11$	$5.82 \pm 0.11$
199.8	$6.53 \pm 0.31$	$5.97 \pm 0.26$
206.8	$6.48 \pm 0.13$	$5.47 \pm 0.11$
211.8	$6.55 \pm 0.31$	$5.70 \pm 0.25$
212.9	$6.41 \pm 0.12$	$5.47 \pm 0.10$
213.9	$6.79 \pm 0.32$	$5.60 \pm 0.24$
215.4	$6.40 \pm 0.19$	$5.26 \pm 0.16$
218.6	$7.16 \pm 0.33$	$5.24 \pm 0.23$
219.6	$7.11 \pm 0.33$	$5.77 \pm 0.25$
220.9	$7.06 \pm 0.14$	$5.33 \pm 0.11$
221.6	$6.95 \pm 0.32$	$5.09 \pm 0.22$
222.7	$6.95 \pm 0.32$	$5.26 \pm 0.23$
223.6	$7.26 \pm 0.33$	$5.49 \pm 0.24$
224.6	$6.95 \pm 0.32$	$5.44 \pm 0.24$

(a)  $10^{-15} \text{ ergs s}^{-1} \text{ cm}^{-2} \text{ \AA}^{-1}$   
(b)  $10^{-13} \text{ ergs s}^{-1} \text{ cm}^{-2}$

**Table 5.** Optical Continuum and H $\beta$  fluxes (cont.)

Julian Date (−2, 450, 000)	$F_{\lambda}$ (5100 Å)	$F(\text{H}\beta)$
(1)	(a) (2)	(b) (3)
225.6	$6.88 \pm 0.32$	$5.33 \pm 0.23$
226.6	$6.87 \pm 0.32$	$5.24 \pm 0.23$
227.8	$6.84 \pm 0.14$	$5.43 \pm 0.11$
231.6	$7.06 \pm 0.32$	$5.69 \pm 0.25$
233.8	$6.82 \pm 0.14$	$5.57 \pm 0.11$
238.3	$6.51 \pm 0.19$	$5.82 \pm 0.17$
240.6	$6.70 \pm 0.31$	$6.04 \pm 0.26$
241.8	$6.67 \pm 0.13$	$5.69 \pm 0.11$
242.6	$6.82 \pm 0.32$	$6.20 \pm 0.27$
248.8	$6.71 \pm 0.13$	$5.47 \pm 0.11$
249.7	$6.30 \pm 0.30$	$5.84 \pm 0.25$
250.7	$6.23 \pm 0.30$	$5.44 \pm 0.24$
251.7	$6.84 \pm 0.32$	$5.92 \pm 0.26$
253.6	$5.85 \pm 0.28$	$5.63 \pm 0.24$
253.8	$6.01 \pm 0.12$	$5.55 \pm 0.11$
254.6	$5.90 \pm 0.29$	$5.84 \pm 0.25$
256.6	$6.43 \pm 0.30$	$5.64 \pm 0.25$
257.7	$6.63 \pm 0.31$	$5.80 \pm 0.25$
258.6	$6.24 \pm 0.30$	$5.30 \pm 0.23$
259.6	$6.04 \pm 0.29$	$5.25 \pm 0.23$
262.8	$6.44 \pm 0.13$	$5.35 \pm 0.11$
270.7	$6.20 \pm 0.30$	$5.27 \pm 0.23$
272.3	$6.83 \pm 0.20$	$5.07 \pm 0.15$
280.6	$6.62 \pm 0.31$	$5.13 \pm 0.22$
281.7	$6.80 \pm 0.32$	$5.53 \pm 0.24$
282.7	$6.05 \pm 0.29$	$5.01 \pm 0.22$
283.7	$6.07 \pm 0.29$	$5.19 \pm 0.22$
284.7	$6.51 \pm 0.31$	$5.36 \pm 0.23$
286.7	$6.86 \pm 0.32$	$5.28 \pm 0.23$
287.6	$6.54 \pm 0.31$	$4.96 \pm 0.22$
288.7	$6.94 \pm 0.32$	$5.30 \pm 0.23$
289.7	$6.46 \pm 0.31$	$5.04 \pm 0.22$
460.1	$6.46 \pm 0.31$	$5.54 \pm 0.24$
465.0	$6.44 \pm 0.30$	$5.55 \pm 0.24$
480.1	$5.98 \pm 0.29$	$5.66 \pm 0.25$
481.1	$6.39 \pm 0.30$	$5.46 \pm 0.24$
482.1	$6.36 \pm 0.30$	$5.75 \pm 0.25$
485.9	$6.51 \pm 0.31$	$5.84 \pm 0.25$
487.0	$6.43 \pm 0.30$	$5.94 \pm 0.26$
489.0	$6.58 \pm 0.31$	$5.79 \pm 0.25$
489.9	$6.79 \pm 0.32$	$5.96 \pm 0.26$
491.0	$6.55 \pm 0.31$	$5.49 \pm 0.24$
494.0	$6.30 \pm 0.30$	$5.42 \pm 0.23$
510.0	$6.66 \pm 0.31$	$5.60 \pm 0.24$
519.8	$6.61 \pm 0.31$	$5.30 \pm 0.23$
546.4	$7.42 \pm 0.22$	$4.88 \pm 0.15$
547.8	$7.61 \pm 0.34$	$5.14 \pm 0.22$
548.8	$7.43 \pm 0.34$	$5.21 \pm 0.23$
549.8	$7.64 \pm 0.34$	$5.39 \pm 0.23$
550.8	$7.64 \pm 0.34$	$5.59 \pm 0.24$
551.8	$7.15 \pm 0.33$	$5.24 \pm 0.23$
552.8	$7.49 \pm 0.34$	$5.55 \pm 0.24$
569.8	$7.55 \pm 0.34$	$5.43 \pm 0.23$

(a)  $10^{-15} \text{ ergs s}^{-1} \text{ cm}^{-2} \text{ \AA}^{-1}$   
(b)  $10^{-13} \text{ ergs s}^{-1} \text{ cm}^{-2}$

**Table 5.** Optical Continuum and H $\beta$  fluxes (cont.)

Julian Date (-2, 450, 000)	$F_\lambda$ (5100 Å)	$F(\text{H}\beta)$
(1)	(a) (2)	(b) (3)
575.4	$7.78 \pm 0.23$	$5.85 \pm 0.17$
578.8	$7.83 \pm 0.35$	$5.37 \pm 0.23$
580.5	$7.39 \pm 0.22$	$5.46 \pm 0.16$
581.8	$7.22 \pm 0.33$	$5.52 \pm 0.24$
582.6	$6.96 \pm 0.32$	$5.57 \pm 0.24$
597.7	$7.08 \pm 0.32$	$5.56 \pm 0.24$
602.6	$6.36 \pm 0.30$	$5.00 \pm 0.22$
604.6	$6.68 \pm 0.31$	$5.22 \pm 0.23$
605.7	$7.11 \pm 0.33$	$4.93 \pm 0.21$
608.7	$7.41 \pm 0.34$	$5.09 \pm 0.22$
609.6	$7.34 \pm 0.33$	$5.35 \pm 0.23$
610.6	$6.88 \pm 0.32$	$4.99 \pm 0.22$
627.6	$7.45 \pm 0.34$	$5.35 \pm 0.23$
628.6	$7.58 \pm 0.34$	$5.51 \pm 0.24$
629.7	$8.26 \pm 0.36$	$5.83 \pm 0.25$
630.7	$7.92 \pm 0.35$	$5.98 \pm 0.26$

(a)  $10^{-15}$  ergs s $^{-1}$  cm $^{-2}$  Å $^{-1}$ (b)  $10^{-13}$  ergs s $^{-1}$  cm $^{-2}$